PCCP

ROYAL SOCIETY OF CHEMISTRY

PAPER

View Article Online
View Journal | View Issue



Cite this: *Phys. Chem. Chem. Phys.*, 2024, **26**, 12869

# Unraveling the origin of the high photocatalytic properties of earth-abundant $TiO_2/FeS_2$ heterojunctions: insights from first-principles density functional theory†

Oluwayomi F. Awe, [a] Henry I. Eya, [a] Ricardo Amaral, [a] Nikhil Komalla, [a] Pascal Nbelayim[b] and Nelson Y. Dzade *[a]

Received 13th September 2023,
Accepted 28th March 2024

DOI: 10.1039/d3cp04453j

rsc.li/pccp

Herein, first-principles density functional theory calculations have been employed to unravel the interfacial geometries (composition and stability), electronic properties (density of states and differential charge densities), and charge carrier transfers (work function and energy band alignment) of a $TiO_2(001)/FeS_2(100)$ heterojunction. Analyses of the structure and electronic properties reveal the formation of strong interfacial Fe–O and Ti–S ionic bonds, which stabilize the interface with an adhesion energy of −0.26 eV $Å^{-2}$. The work function of the $TiO_2(001)/FeS_2(100)$ heterojunction is predicted to be much smaller than those of the isolated $FeS_2(100)$ and $TiO_2(001)$ layers, indicating that less energy will be needed for electrons to transfer from the ground state to the surface to promote photochemical reactions. The difference in the work function between the $FeS_2(100)$ and $TiO_2(001)$ heterojunction components caused an electron density rearrangement at the heterojunction interface, which induces an electric field that separates the photo-generated electrons and holes. Consistently, a staggered band alignment is predicted at the interface with the conduction band edge and the valence-band edge of $FeS_2$ lying 0.37 and 2.62 eV above those of anatase. These results point to efficient charge carrier separation in the $TiO_2(001)/FeS_2(100)$ heterojunction, wherein photo-induced electrons would transfer from the $FeS_2$ to the $TiO_2$ layer. The atomistic insights into the mechanism of enhanced charge separation and transfer across the interface rationalize the observed high photocatalytic activity of the mixed $TiO_2(001)/FeS_2(100)$ heterojunction over the individual components.



## I. Introduction

Rising global energy demand and related environmental pollution issues are among the greatest technological challenges facing humanity in the 21st century. To ensure environmental sustainability and the long-term development of human society, there is a pressing need for the development of environmentally friendly and renewable technologies for green energy production and environmental remediation. Among the various emerging technologies, semiconductor-based photocatalysis has immense potential owing to its ability to directly utilize the abundant and freely available solar energy for both the production of valuable chemical fuels, such as hydrogen and hydrocarbon fuels, and the degradation of harmful pollutants.[1–6]

The development of inexpensive, highly stable, and recyclable photocatalysts with large specific surface areas and high photocatalytic activity is the key to the large-scale implementation of photocatalytic technology. In the past decade, several photocatalytic materials including $TiO_2$,[7,8] g-$C_3N_4$,[9] $Ga_2O_3$,[10] $ZnIn_2S_4$,[11] $Bi_2WO_6$,[12] $SrNb_2O_6$,[13] and ZnO[14] have been developed. Among them, $TiO_2$ has attracted the most attention as an active photocatalyst for several environmental and energy applications owing to its abundance, low cost, chemical stability, non-toxicity, and resistance toward photocorrosion.[15,16] However, the restricted light absorption ability (3–5% of the entire sunlight spectrum) owing to the wide band gap (3.2–3.35 eV) and the fast recombination of photogenerated electron–hole pairs remain as two major factors that limit the practical applications of $TiO_2$.[17] To overcome these limitations and promote efficient separation of photogenerated charge carries, various strategies including doping,[18] metal loading,[19] surface modification,[20] and introducing heterojunctions[21] have been adopted.

Among the various strategies explored to efficiently separate the photogenerated electron–hole pairs in semiconductor photocatalysts, heterojunction formation using different functional

[a] Department of Energy and Mineral Engineering, Pennsylvania State University, University Park, PA 16802, USA
[b] Department of Materials Science and Engineering, School of Engineering Sciences, College of Basic and Applied Sciences, University of Ghana, Accra, Ghana.
E-mail: nxd5313@psu.edu

† Electronic supplementary information (ESI) available. See DOI: https://doi.org/10.1039/d3cp04453j

materials in a single photocatalyst has been proven to be one of the most effective strategies.[22–26] The combined beneficial synergistic effects in heterojunction photocatalysts (particularly, properly engineered type-II band aligned heterojunctions) have he potential for broadening light harvesting properties, improving chemical stability, promoting the efficient separation and transfer of charge carriers to the appropriate active sites for the desired redox reactions, and thus boosting photocatalytic activity.[22,27] Therefore, photoelectrochemical devices based on dual absorbers (heterojunctions) can achieve thermodynamic efficiencies of up to 41% for water splitting and 32–42% for $CO_2$ reduction.[28–30] For instance, enhanced photocatalytic activity has been reported for $Cu_2O/TiO_2$,[31] $WO_3/TiO_2$,[32–34] $TiO_2/CdS$,[35,36] and $TiO_2/CsPbBr_3$[37] heterojunctions.

Pyrite ($FeS_2$) is a potential earth-abundant and non-toxic cocatalyst for next-generation photoelectrochemical (PEC) applications owing to its narrow band gap (0.95 eV) and large optical absorption coefficient ($>10^5$ $cm^{-1}$).[38] Furthermore, $FeS_2$ displays great stability against photocorrosion in photoelectrochemical (PEC) applications.[39,40] Because the coupling of $FeS_2$ with a large band gap semiconductor like $TiO_2$ can promote the efficient separation of photogenerated carriers, the fabrication of $TiO_2/FeS_2$ heterojunction photocatalysts has recently been explored for photoelectrocatalytic reduction of $CO_2$ to methanol under visible light,[41] the hydrogen evolution reaction (HER),[39,42] the oxygen evolution reaction (OER),[43] and photocatalytic degradation of organic compounds.[44] The $TiO_2/FeS_2$ heterojunction photocatalysts show enhanced photocatalytic activity compared with the corresponding single photocatalysts. For instance, the formation of $FeS_2$/anatase-$TiO_2$ core/shell composites has been demonstrated to enhance hydrogen production by methanol/water (1 : 1) due to a narrower band gap than those of isolated $TiO_2$ and $FeS_2$.[45] Furthermore, the coupling of pyrite $FeS_2$ with hierarchical top-porous bottom-tubular $TiO_2$ nanotubes has been applied to realize PEC performance enhancement by more than 3-orders of magnitude from the ultraviolet and visible light regions compared to that of the isolated $TiO_2$ nanotubes.[46] However, the origin of the enhanced photocatalytic performance is not well known and there have been no comprehensive theoretical studies dedicated to uncovering the detailed mechanism of carrier dynamics of $FeS_2$-based heterostructures. It is, therefore, highly desirable to investigate the factors influencing the photocatalytic properties of the $TiO_2/FeS_2$ composite and the nature of the interfacial interactions between them.

In this work, first-principles density functional theory (DFT) calculations have been employed to unravel the interfacial structure and stability, density of states, differential charge densities, work function, and energy band alignment of the $TiO_2(001)/FeS_2(100)$ heterojunction. The $TiO_2/FeS_2$ heterojunction is demonstrated to be stabilized by the formation of interfacial Fe–O and Ti–S ionic bonds. A staggered band alignment with a small conduction band offset of 0.37 eV is predicted for the $TiO_2(001)/FeS_2(100)$ heterojunction, which is small enough to promote the efficient separation of photogenerated electrons from $FeS_2$ to $TiO_2$ under light irradiation. Consistently, a lower work function is predicted for the $FeS_2(100)$ surface ($\phi$ = 5.03 eV) than the $TiO_2(001)$ surface ($\phi$ = 5.22 eV). Compared to the isolated materials, the $TiO_2(001)/FeS_2(100)$ heterojunction has a much lower work function ($\phi$ = 4.09 eV), which should promote the easy transfer of electrons to the photocatalyst surface for photochemical reactions. The efficient separation of electron–hole pairs in the $TiO_2(001)/FeS_2(100)$ junction is beneficial for improving the photocatalytic activity, explaining well the high-photocatalytic performances reported in previous experimental investigations.

## II. Computational details

The first-principles calculations were performed using the plane augmented-wave (PAW)[47] as implemented in the Vienna Ab initio Simulation Package (VASP).[48,49] Geometry optimizations were performed using the PBE (Perdew–Burke–Ernzerhof) generalized gradient approximation functional[50] until the residual forces on all atoms reached $10^{-3}$ eV Å$^{-1}$. The kinetic plane-wave energy cut-off was set to 600 eV, which converged the total energies of the studied materials to within $10^{-6}$ eV. Non-local dispersion forces were accounted for using the Grimme DFT-D3 scheme.[51] Monkhorst–Pack[52] $k$-points meshes of (7 × 7 × 7) and (9 × 9 × 5) were used to sample the Brillouin zone of $FeS_2$ and $TiO_2$, respectively. The pyrite $FeS_2$ was modeled in the cubic $Pa3$ space group, whereas anatase $TiO_2$ was modeled in

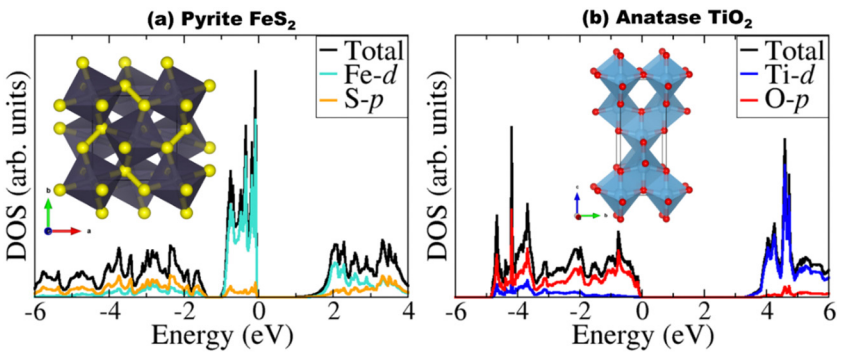


Fig. 1 The total and partial density of states of (a) pyrite $FeS_2$ and (b) anatase $TiO_2$. The Fermi level is set to zero. The insets are the optimized crystal structures in polyhedral representation.

 

the tetragonal $I4_1/amd$ space group as shown in Fig. 1. To accurately predict the electronic bandgap of $FeS_2$ and $TiO_2$, we have used the Hubbard correction (DFT+$U$) approach,[53] which adds an on-site Coulomb repulsion to the DFT Hamiltonian, providing a better treatment of the strong electron correlation in the localized Fe and Ti d-orbitals. An effective $U$ of 2.0 eV for Fe-3d in $FeS_2$ and that of 7.3 eV for Ti-3d in $TiO_2$ have been tested to provide an accurate description of the structural parameters and the electronic bandgaps. Fig. S1 and S2 (ESI†) show the variation of the bandgap and lattice parameters calculated at different effective $U$-values.

The $FeS_2$(100) and $TiO_2$(001) surfaces were coupled together to form the $TiO_2$(001)/$FeS_2$(001) heterojunction because they are often reported as the stable surfaces and they do not contain dangling bonds that could lead to the formation of a non-coherent interface.[54,55] A vacuum region of 20 Å was added to the $c$-direction to avoid spurious interactions between periodic slabs. The work function ($\Phi$), which represents the minimum energy needed to remove an electron from the bulk of a material through a surface to a point outside the material, was calculated as $\Phi = E_{vac} - E_F$, where $E_{vac}$ is the vacuum level and $E_F$ is the Fermi level. Dipole corrections perpendicular to all surfaces were accounted for using the Makov–Payne scheme,[56] which ensured that there is no net dipole perpendicular to the surfaces that may affect the potential in the vacuum level. Charge transfer between the $FeS_2$(100) and $TiO_2$(001) slabs in the $TiO_2$(001)/$FeS_2$(001) heterojunction is quantified using the Bader charge analysis code developed by Henkelman and coworkers.[57]

# III. Results and discussion

## A. Structural and electronic properties of bulk $FeS_2$ and $TiO_2$

Pyrite $FeS_2$ crystallizes in the cubic $Pa3$ space group.[58] The cubic pyrite structure can be described as trigonally distorted $FeS_6$ octahedra and tetrahedrally coordinated sulfur atoms (inset in Fig. 1a).[58–61] The lattice parameter of $FeS_2$ is predicted at $a$ = 5.409 Å in close agreement with the experimental value (5.416 Å)[62,63] and a range of earlier theoretical results of pyrite.[64–68] The Fe–S and S–S bond distances in pyrite are calculated as 2.252 and 2.159 Å, respectively.

Anatase $TiO_2$ crystallizes in the tetragonal structure with the space group $I4_1/amd$ symmetry (inset in Fig. 1b).[69,70] The structure consists of distorted $TiO_6$ octahedra sharing two adjacent edges so that infinite planar double chains are formed. In the $ab$-plane, every O ion has neighboring Ti ions either in the $a$ or the $b$ directions. The equilibrium lattice parameters of anatase $TiO_2$ are predicted at $a$ = 3.803 Å and $c$ = 9.517 Å, in good agreement with the experimental lattice parameters ($a$ = 3.785 Å and $c$ = 9.514 Å).[70] The electronic density of states projected (PDOS) on the Fe d-states and S p-states of $FeS_2$ is displayed in Fig. 1a. An analysis of the PDOS of $FeS_2$ reveals that the valence and conduction band edges are composed mainly of the Fe 3d states with a small contribution of the S 3p states, indicating that the pyrite Fe 3d → Fe 3d charge transfer semiconductor is in good agreement with earlier theoretical predictions.[64,71] The band gap of pyrite is calculated to be 0.96 eV, in good agreement with the value obtained from photoconductivity measurements (0.90–1.00 eV).[38,72,73] The electronic PDOS of anatase $TiO_2$ is

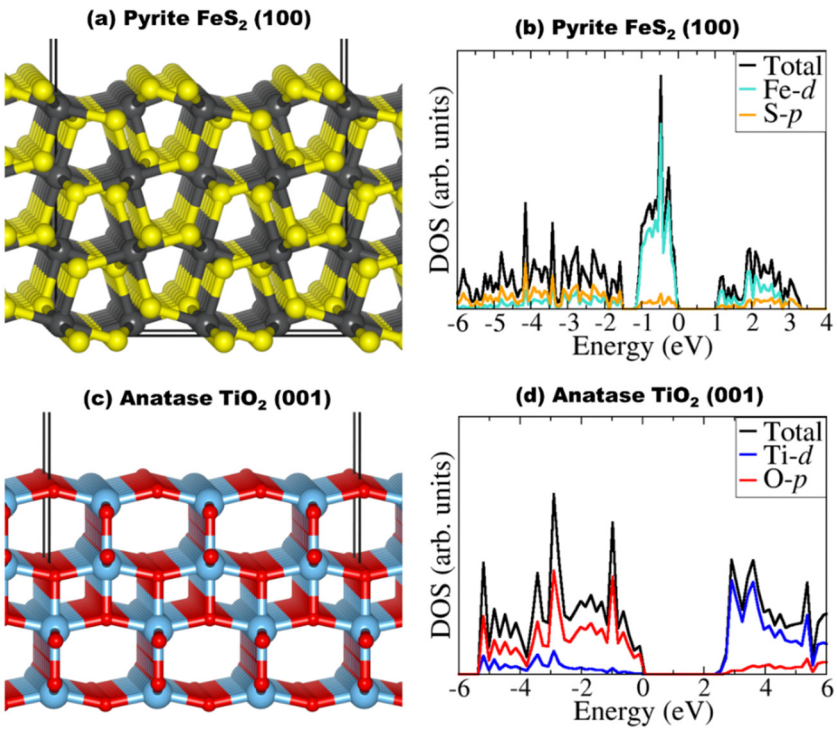


Fig. 2 Surface structures and the corresponding total and partial density of states (PDOS) of (a–b) $FeS_2$(100) and (c–d) $TiO_2$(001) surface models. The Fermi level is set to zero.

shown in Fig. 1b, wherein the valence band edge is dominated by O 2p, and the conduction band edge is dominated by Ti 3d states. The electronic band gap of anatase $TiO_2$ is predicted to be 3.21 eV, in good agreement with the experimental value of 3.23 eV.[74]

The pyrite $FeS_2(100)$ and anatase $TiO_2(001)$ surfaces (Fig. 2a and b), which have been investigated extensively in previous studies[75–78] because of their stability and expression in the morphology of their respective crystals,[79,80] were employed as a reference for comparison with the interface models, wherein we analyze the interactions between these two surfaces. The electronic project density of states (PDOS) of the pyrite $FeS_2(100)$ and anatase $TiO_2(001)$ are shown in Fig. 2c and d, respectively. The semiconductor characters of both $FeS_2$ and $TiO_2$ were observed with the bandgaps computed at 0.96 eV and 2.46 eV, respectively. The reduction in the $TiO_2(001)$ surface compared to the bulk value can be rationalized by considering the fact that the change in the coordination of the surface atoms compared to those in the bulk modifies the shape of the bands of the O 2p and Fe 3d hybridization, which consequently reduce the bandgap.

### B. Structural, electronic and optical properties of the $TiO_2(001)/FeS_2(100)$ heterojunction

Considering their surface stabilities and reasonable lattice match, the $FeS_2(100)$ and $TiO_2(001)$ surfaces were employed in building the $TiO_2(001)/FeS_2(100)$ interface model. The $FeS_2(100)$ unit cell was placed on the relaxed $TiO_2(001)$ surface and adjusted along the interfacial plane to fit the substrate's lattice parameters. A $(2 \times 2)$ supercell of the $FeS_2(100)$ surface $(10.808 \times 10.808)$ and a $(3 \times 3)$ supercell of the $TiO_2(001)$ surface $(11.588 \times 11.588)$ were employed, which yield a small lattice mismatch of 6.73% in both the $x$ and $y$ directions in the interface of $FeS_2(100)$ epi-layer and a $TiO_2(001)$ substrate. Fig. 3a shows that the $TiO_2(001)/FeS_2(100)$ interface is stabilized through the formation of Fe–O and Ti–S bonds. The average Fe–O and Ti–S bond distances are predicted to be 2.176 Å and 2.634 Å, respectively, which are short enough, in particular the Fe–O bonds, to stabilize the interface structure.

The interfacial adhesion energy ($E_{ad}$) was calculated to ascertain the stability of the $TiO_2(001)/FeS_2(100)$ interface. It is defined as $E_{ad} = (E_{TiO_2/FeS_2} - (E_{TiO_2} + E_{FeS_2}))/S$, where $E_{TiO_2/FeS_2}$ is the total energy of the $TiO_2/FeS_2$ heterojunction with the interface surface area $S$, while $E_{TiO_2}$ and $E_{FeS_2}$ are the total energies of the $TiO_2$ and $FeS_2$ surfaces, respectively. The interface adhesion energy between the $TiO_2(001)$ and $FeS_2(100)$ surfaces was predicted to be $-0.26$ eV Å$^{-2}$, which indicates that the interface structure is thermodynamically stable. To understand the charge transfer and bonding type in the $TiO_2(001)/FeS_2(100)$ nanocomposite, the differential charge density iso-surface contours are determined as shown in Fig. 3b. The formation of a stable interface is evident by the accumulation of charges between the Fe–O and Ti–S atoms. Further insight into the bonding nature at the $TiO_2(001)/FeS_2(100)$ interface was gained by determining the electron localization function plots as shown in Fig. 4. It can be evident from Fig. 4a that the electron clouds are localized around S and O atoms (yellow color) and delocalized from Fe and Ti atoms, suggesting ionic bonds in both $FeS_2$ and $TiO_2$. In the two-dimensional electron localization function (Fig. 4b), the

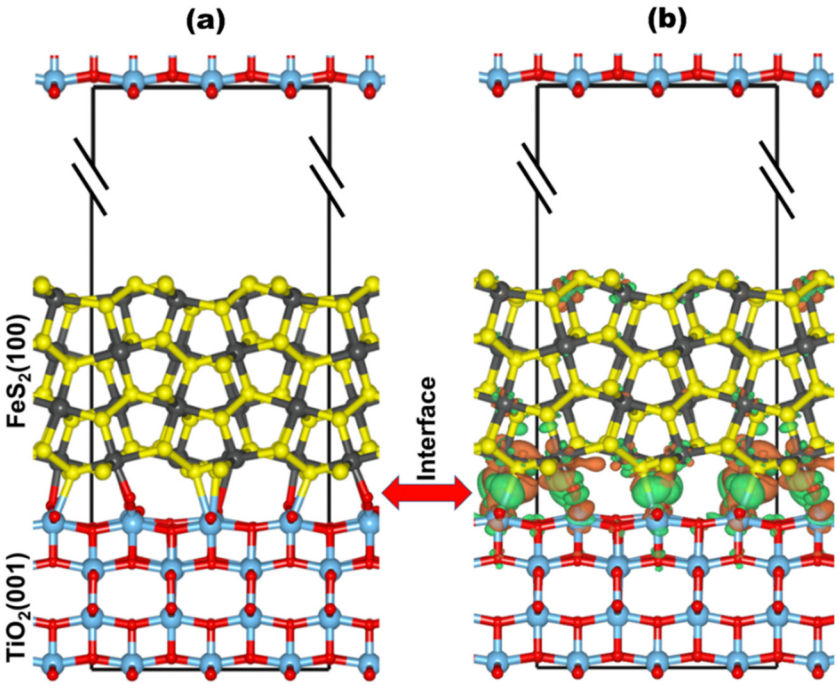


Fig. 3 (a) The optimized structure of the $FeS_2(100)$–$TiO_2(001)$ interface model and (b) the differential charge density iso-surface contours with an iso-value of 0.01 eV Å$^{-3}$ showing electron density accumulation (green) and depletion (orange) within the interface region.

 

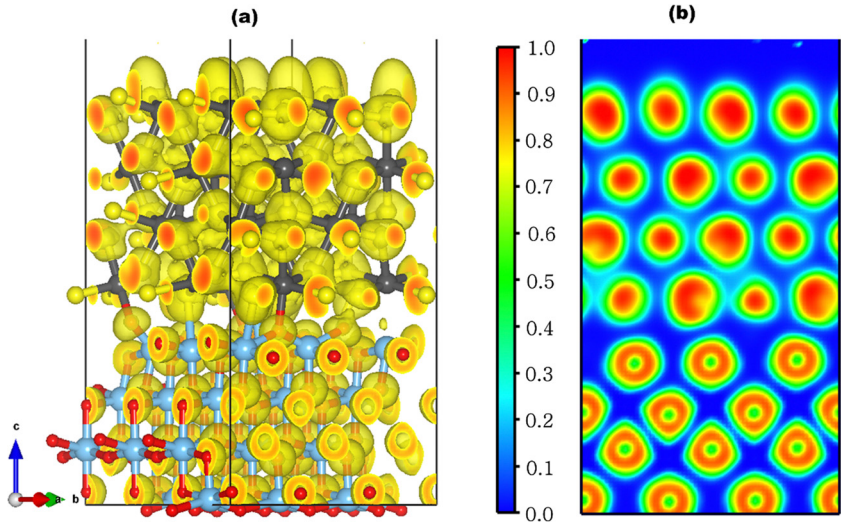


Fig. 4 The three-dimensional (a) and two-dimensional (b) electron localization function plots of the $FeS_2$(100)–$TiO_2$(001) interface. The isosurfaces in (a) are determined at an iso-value of 0.72 eV Å$^{-3}$ and clearly show the electron distributions are localized around O and S atoms. In (b), the blue and red regions denote low and high electron localization, respectively. ELF values of 0 and 1 correspond to perfect delocalization and localization, respectively.

localized electron clouds on the $FeS_2$ interface atoms do not connect with those of the $TiO_2$ interface atoms, which suggests the formation of Fe–O and Ti–S atom ionic bonds at the $TiO_2$(001)/$FeS_2$(100) interface.

Furthermore, Bader charge analysis (Table S1, ESI†) was carried out to quantify any charge transfer between the $FeS_2$(100) and $TiO_2$(001) layers when they are coupled together. A total charge of 0.87 e$^-$ is predicted to be transferred from the $FeS_2$(100) layer to the top of the $TiO_2$(001) layer. The work functions ($\Phi$) of $FeS_2$(100) and $TiO_2$(001) surfaces were calculated to help understand the origin of the charge transfer across the interface. The work function of the $FeS_2$(100) surface is 5.03 eV *vs.* vacuum as shown in Fig. 5a, which is in excellent agreement with the value of 5.0 eV obtained from ultraviolet photoelectron spectroscopy measurements.[38,81] As shown in Fig. 5b, the work function of the $TiO_2$(001) surface is 5.22 eV, which is larger than that of the $FeS_2$(100) surface and is consistent with experimental results (5.1 eV).[82] Therefore, the spontaneous interfacial charge transfer from the $FeS_2$(100) layer to the $TiO_2$(001) layer when they are coupled together can be rationalized by the higher work function of the $TiO_2$(001) surface.

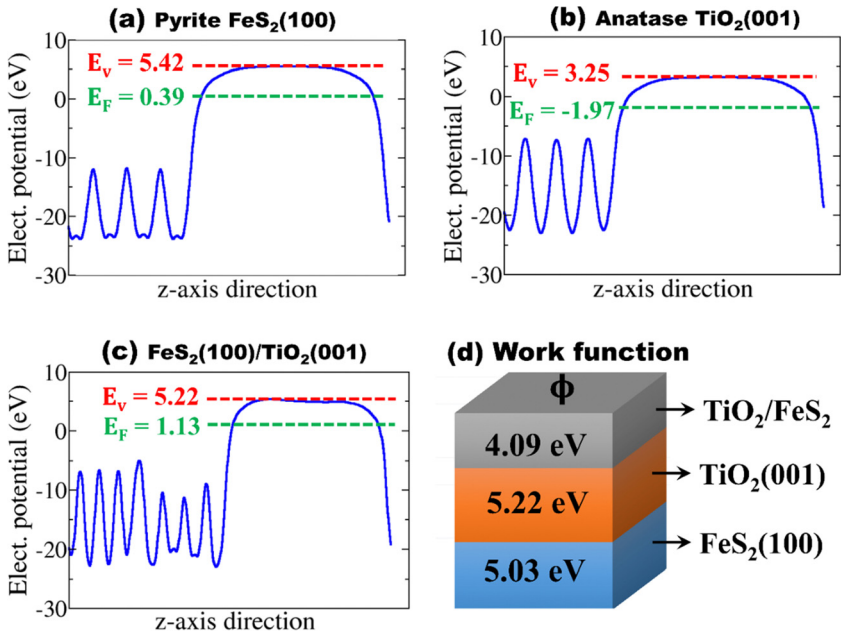


Fig. 5 The electrostatic potentials for the (a) $FeS_2$(100) surface, (b) $TiO_2$(001) surface, and (c) $FeS_2$(100)–$TiO_2$(001) nanocomposite. The red and green dashed lines represent the vacuum level ($E_v$) and the Fermi level ($E_F$), respectively. (d) Work function ($\phi = E_v - E_F$).

Generally, when two photocatalytic materials are coupled to fabricate heterojunction photocatalysts, the electrons tend to transport from the material with the lower work function (where they are less tightly bound) and travel to the higher work function material. The work function difference between the components of the heterojunction causes a rearrangement of electron density at the heterojunction interface (Fig. 3b) and results in an induced electric field that separates the oppositely charged photo-generated electrons and holes. The work function of the $TiO_2(001)/FeS_2(100)$ heterojunction calculated to be 4.09 eV *vs.* vacuum as shown in Fig. 5c is lower than those of isolated $FeS_2(100)$ and $TiO_2(001)$ surfaces. As the value of the photocatalyst work function dictates its ability to easily transfer electrons and thus its photoactivity, the predicted lower work function for the $TiO_2(001)/FeS_2(100)$ heterojunction is the origin of the observed enhanced photocatalytic performances.[31–36]

To further ascertain the effect of coupling $FeS_2(100)$ and $TiO_2(001)$ on the photocatalytic performance, the layer-resolved projected density of states of the $TiO_2(001)/FeS_2(100)$ heterojunction was determined as shown in Fig. 6. The PDOS indicates the presence of strong interfacial interactions between $FeS_2(100)$ and $TiO_2(001)$. Compared to the isolated surface models (Fig. 2), it is worth noting that the variations in the interface PDOS are particularly strong in the $TiO_2(001)$ layer (L4) interacting with the $FeS_2(100)$ surface. We observe a reduction in the bandgap of the $TiO_2(001)$ layers towards the interface region, calculated to be 3.07, 2.70, 2.45, and 1.11 eV for L1, L2, L3, and L4, respectively. The reduction and the changes in the features of the PDOS of the $TiO_2(001)$ interface layer (L4) can be rationalized by considering the fact that the interactions between Fe 3d and O 2p states at the interface (average Fe–O = 2.176 Å) are much stronger than between Ti 3d and S 2p states (average Ti–S = 2.634 Å). The stronger interface Fe–O bond formation resulted in the pulling up of the interacting O atoms towards the interface $FeS_2$ layer (L5) by 0.521–0.696 Å. However, due to the weaker interface Ti–S bonds, the S atoms remained negligibly displaced upward/down, which is consistent with small variations observed in the PDOS features and bandgaps of the different $FeS_2(100)$ layers, which remained at 1.1 eV. These results indicate that the electronic structure and bandgap of $TiO_2$ can be modified by the introduction of $FeS_2$ thin films.

Considering that the optical absorption properties of photocatalysts are of great importance for their photocatalytic activity, we have determined the absorption spectra of isolated $FeS_2(100)$ and $TiO_2(001)$ and compared them with that of the $TiO_2(001)/FeS_2(100)$ heterojunction as shown in Fig. 7. The linear absorption properties were calculated from the frequency-dependent complex dielectric function $\varepsilon(w)$ and expressed as $\varepsilon(w) = \varepsilon_1(w) + i\varepsilon_2(w)$, where $\varepsilon_1(w)$ and $\varepsilon_2(w)$ are the real and imaginary parts of the dielectric function, respectively, and $w$ is the photon frequency. The absorption coefficient $\alpha(w)$ is calculated from $\varepsilon_1(w)$ and $\varepsilon_2(w)$ as follows:

$$\alpha(w) = \frac{\sqrt{2w}}{c}\left[\sqrt{\varepsilon_1^2 + \varepsilon_2^2} - \varepsilon_1\right]^{\frac{1}{2}} \quad (1)$$

Compared to isolated $TiO_2(001)$, the optical absorption edge of the $TiO_2(001)/FeS_2(100)$ heterojunction is clearly red-shifted to lower photon energy with a higher absorption intensity observed in the visible-light region. Consistent with its lower bandgap, the $FeS_2(100)$ surface shows the highest absorption intensity. The enhancement in the optical absorption of $TiO_2(001)$ when coupled with $FeS_2(100)$ suggests improvement in the photocatalytic activity of the heterojunction.

### C. Band alignment at the $TiO_2(001)/FeS_2(100)$ interface

The band alignment of the heterojunction is of fundamental importance to achieve an efficient charge carrier separation, *i.e.*, to reduce electron–hole recombination and improve photoactivity. Thus, an accurate prediction of the nature of band alignment and offsets of valence and conduction bands in the heterojunction is of key importance. Herein, the band alignment at the $TiO_2(001)/FeS_2(100)$ interface has been estimated by the potential line-up method.[83,84] The first step requires the determination of the electronic structure (density of states or band structure) calculation for the bulk materials.[85] From the bulk electronic structure, the position of the valence-band

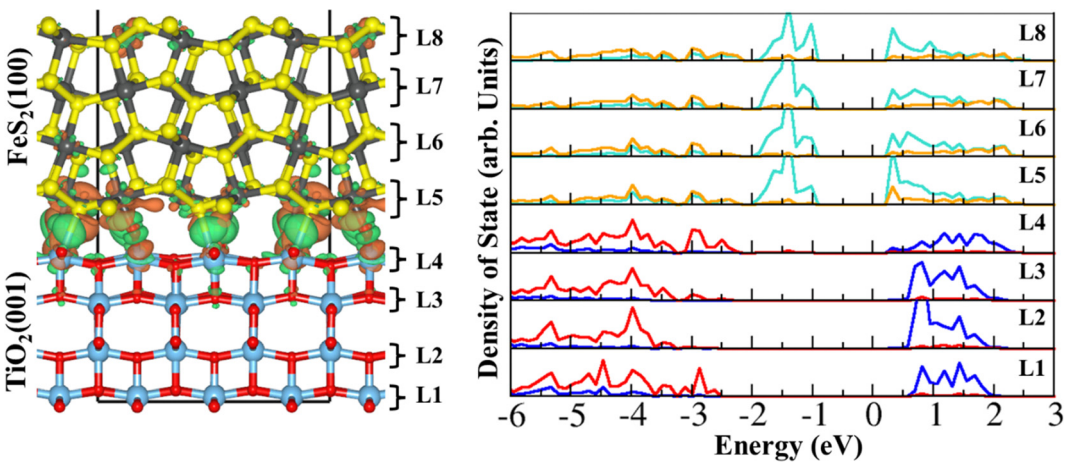


Fig. 6 The calculated layer-resolved density of states (PDOS) for the $FeS_2(100)$–$TiO_2(001)$ heterojunction. The Fermi level is set to zero.

 

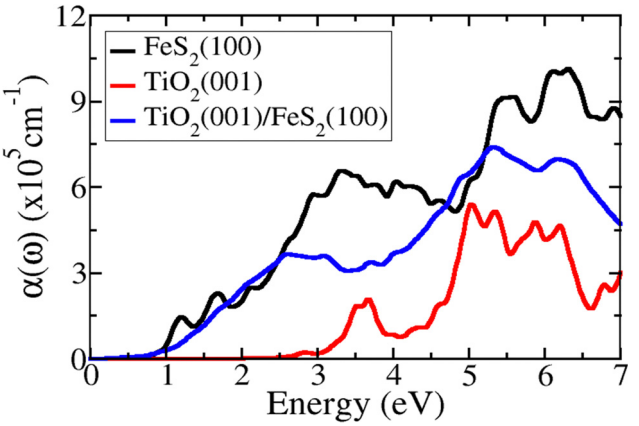


Fig. 7 Calculated optical absorption spectra of $FeS_2$(100), $TiO_2$(001), and $FeS_2$(100)–$TiO_2$(001) heterojunctions as a function of photon energy.

maximum (VBM) can be determined with respect to the average electrostatic potential in the infinite solid. However, the average electrostatic potential is not properly defined for bulk calculations using periodic boundary conditions.[86] To obtain an appropriate reference for aligning the valence and conduction bands, a superlattice calculation is performed, which allows aligning the electrostatic potentials in the bulk-like regions of the two materials, as shown in Fig. 8a. The space-dependent electrostatic potential $V(\bar{r})$ is calculated by solving the Poisson equation. The planar-averaged potential $\bar{V}(z)$ across the interface was obtained by the following equation:

$$\bar{V}(z) = \frac{1}{S}V(\bar{r})\mathrm{d}x\mathrm{d}y, \quad (2)$$

where $S$ is the interface surface area parallel to the $x$–$y$ plane. This planar-average potential exhibits periodic oscillations along the $z$ axis due to the spatial distribution of the electrons and ionic cores. These bulk-like oscillations in the $\bar{V}(Z')$ with respect to the $z$-direction in the two phases can be removed by determining the macroscopic average potential $\bar{\bar{V}}(z)$, which is given by:

$$\bar{\bar{V}}(z) = \frac{1}{L}\int_{Z-L/2}^{Z+L/2}\bar{V}(z')\mathrm{d}z', \quad (3)$$

where $L$ is the oscillation period of $\bar{V}(Z')$. Using the macroscopic average $\bar{\bar{V}}(z)$ as in ref. 85 and 87, the valence band offset ($\Delta E_{VBO}$) at the $TiO_2$(001)/$FeS_2$(100) heterojunction was determined as follows:

$$\Delta E_{VBO} = \Delta\bar{\bar{V}}(z)_{TiO_2/FeS_2} + \left(\bar{\bar{V}}(z) - E_{VMB}\right)_{FeS_2} - \left(\bar{\bar{V}}(z) - E_{VMB}\right)_{TiO_2}, \quad (4)$$

where $\Delta\bar{\bar{V}}(z)$ denotes the difference of $\bar{\bar{V}}(z)$ between the two materials in the heterojunction as shown in Fig. 8a. The last two terms denote the difference between the valence band maximum energy ($E_{VBM}$) and $\bar{\bar{V}}(z)$ of the corresponding isolated materials in the heterojunction. The conduction-band offset ($\Delta E_{CBO}$) at the $TiO_2$(001)/$FeS_2$ (100) can be calculated using the

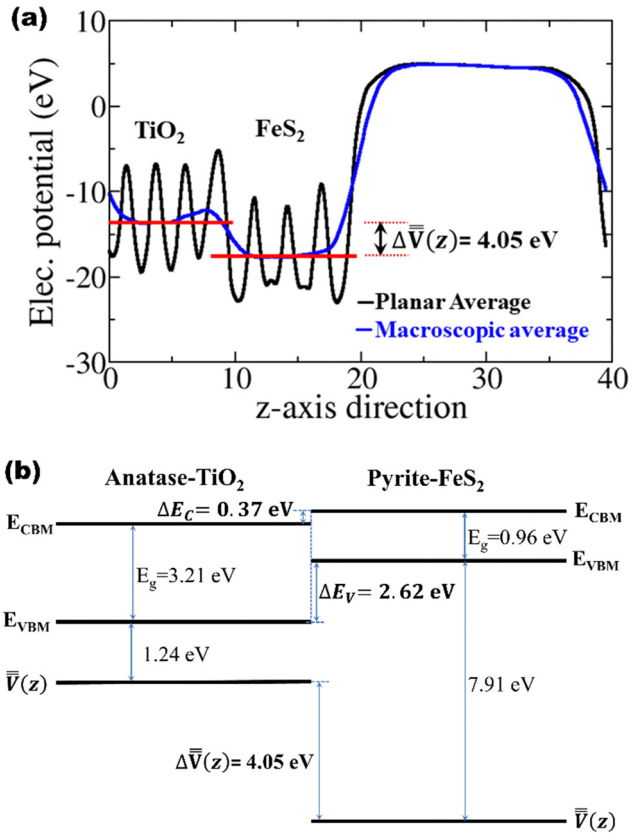


Fig. 8 (a) Electrostatic potential profile of the $TiO_2$(001)/$FeS_2$(100) interface along the [001] direction. The black solid line denotes the planer average whereas the blue solid line represents the macroscopic average of the electrostatic potential across the interface and $\Delta\bar{\bar{V}}(z)$ stands for the resulting line up. (b) Schematic band alignment diagram of the $TiO_2$(001)/$FeS_2$(100) heterojunction.

following formula:

$$\Delta E_{CBO} = E_g^{TiO_2} - E_g^{FeS_2} - \Delta E_{VBO}, \quad (5)$$

where the first two items in eqn (4) represent the band gaps of the bulk $TiO_2$ and $FeS_2$.

The macroscopic average ($\bar{\bar{V}}(z)$) values of $FeS_2$ and $TiO_2$ far away from the interface of the $TiO_2$(001)/$FeS_2$(100) heterojunction are −17.67 and −13.62 eV, respectively, giving rise to a $\Delta\bar{\bar{V}}(z)$ value of 4.05 eV. The energy differences between the macroscopic average potential and the VBM for the bulk $TiO_2$ and $FeS_2$ are calculated to be 1.24 eV and 7.91 eV, respectively. Based on eqn (3), the $\Delta E_{VBO}$ value at the $FeS_2$/$TiO_2$ heterojunction is determined to be 2.62 eV, whereas the $\Delta E_{CBO}$ value is calculated to be 0.37 eV based on eqn (4). As schematically shown in Fig. 8b, the band alignment shows both the VBM and CBM of $FeS_2$ to be above that of $TiO_2$, resulting in the formation of a type-II band alignment.

The higher valence and conduction band edges of $FeS_2$ than those of $TiO_2$ suggest that upon irradiation of the $TiO_2$(001)/$FeS_2$(100) heterojunction, photogenerated conduction electrons will transfer from $FeS_2$ to $TiO_2$, and *vice versa* for photogenerated valence holes. The spatial distribution of the photogenerated

electron–hole pairs in the two materials will inhibit their recombination, which is of great benefit for enhancing photocatalytic activity. Consistently, enhanced photocatalytic activity has been reported for methanol under visible light,[41] a hydrogen evolution reaction (HER),[42] an oxygen evolution reaction (OER),[43] and photocatalytic degradation of organic compounds over $FeS_2$/$TiO_2$-based semiconductor composites.[44] Our results on the electronic properties and band alignment characteristics compare well with previous theoretical and experimental investigations that observed type-II band alignment formation at $SrTiO_3$/$TiO_2$,[88] $CeO_2$/$TiO_2$,[89] and $Cu_2O$/$TiO_2$[90] heterojunctions as the primary reason for favoring efficient charge-carrier separation to enhance photocatalytic activity.

## IV. Summary and conclusions

In summary, the interface structure and stability, electronic structure, and charge carrier dynamics in the $TiO_2(001)$/$FeS_2(100)$ heterojunction were unraveled by the first-principles density functional theory methodology. It is demonstrated that the $FeS_2(100)$ surface can form a stable interface with the $TiO_2(001)$ surface *via* strong ionic Fe–O and Ti–S interactions. A strong variation in the interface density of states is observed particularly in the $TiO_2$ region compared to isolated surface models, which can be ascribed to the stronger Fe–O bonds and surface reconstruction induced by the introduction of $FeS_2$. Based on calculated electronic work functions and predicted type-II staggered band alignments at the $TiO_2(001)$/$FeS_2(100)$ interface with both the conduction band edge and the valence-band edge of $FeS_2$ lying above that of $TiO_2$, efficient separation and transfer of photogenerated charge carriers from the $FeS_2$ layer to the $TiO_2$ layer would occur. The migration of electrons to the $TiO_2$ layer is also expected to enhance its stability by keeping it in a reduced state. The atomic-level insights provided into the structure and interfacial phenomena in $TiO_2(001)$/$FeS_2(100)$ heterojunctions rationalizes the often-observed enhancement of photocatalytic performance and provides promising strategies for designing and engineering more efficient $TiO_2$-based photocatalysts.

## Conflicts of interest

There are no conflicts to declare.

## Acknowledgements

The authors acknowledge the support of the College of Earth and Mineral Sciences and the John and Willie Leone Family Department of Energy and Mineral Engineering of Pennsylvania State University. This research was supported in part by a Seed Grant award from the Penn State Institute for Computational and Data Sciences and the Institutes of Energy and the Environment. Pascal Nbelayim acknowledges support from the University of Ghana Building a New Generation of Academics in Africa (BANGA-Africa) Project Seed Research Grant [UG-BA/SRG-008/2022] with funding from the Carnegie Corporation in New York. Computations for this research were performed on the Pennsylvania State University's Institute for Computational and Data Sciences' Roar supercomputer.

## References

1 G. C. Xie, K. Zhang, B. D. Guo, Q. Liu, L. Fang and J. R. Gong, Graphene-based materials for hydrogen generation from light-driven water splitting, *Adv. Mater.*, 2013, **25**, 3820–3839.
2 A. Kudo and Y. Miseki, Heterogeneous photocatalyst materials for water splitting, *Chem. Soc. Rev.*, 2009, **38**, 253–278.
3 M. Marszewski, S. Cao, J. Yub and M. Jaroniec, Semiconductor-based photocatalytic $CO_2$ conversion, *Mater. Horiz.*, 2015, **2**, 261–278.
4 H. Tong, S. Ouyang, Y. Bi, N. Umezawa, M. Oshikiri and J. Ye, Nano-photocatalytic materials: possibilities and challenges, *Adv. Mater.*, 2012, **24**, 229–251.
5 U. I. Gaya and A. H. Abdullah, Heterogeneous photocatalytic degradation of organic contaminants over titanium dioxide: A review of fundamentals, progress, and problems, *J. Photochem. Photobiol., C*, 2008, **9**, 1–12.
6 A. Fujishima, X. Zhang and D. A. Tryk, $TiO_2$ photocatalysis and related surface phenomena, *Surf. Sci. Rep.*, 2008, **63**, 515–582.
7 A. Fujishima and K. Honda, Electrochemical photolysis of water at a semiconductor electrode, *Nature*, 1972, **238**, 37–38.
8 J. Schneider, M. Matsuoka, M. Takeuchi, J. Zhang, Y. Horiuchi, M. Anpo and D. W. Bahnemann, Understanding $TiO_2$ Photocatalysis: Mechanisms and Materials, *Chem. Rev.*, 2014, **114**(19), 9919–9986.
9 W.-J. Ong, L.-L. Tan, Y. H. Ng, S.-T. Yong and S.-P. Chai, Graphitic Carbon Nitride (g-$C_3N_4$)-Based Photocatalysts for Artificial Photosynthesis and Environmental Remediation: Are We a Step Closer to Achieving Sustainability?, *Chem. Rev.*, 2016, **116**(12), 7159–7329.
10 M. Akatsuka, Y. Kawaguchi, R. Itoh, A. Ozawa, M. Yamamoto, T. Tanabe and T. Yoshida, Preparation of $Ga_2O_3$ photocatalyst highly active for $CO_2$ reduction with water without cocatalyst, *Appl. Catal., B*, 2020, **262**, 118247.
11 S. Wang, B. Guan and X. W. D. Lou, Construction of $ZnIn_2S_4$–$In_2O_3$ Hierarchical Tubular Heterostructures for Efficient CO2 Photoreduction, *J. Am. Chem. Soc.*, 2018, **140**, 5037–5040.
12 S. Cao, B. Shen, T. Tong, J. Fu and J. Yu, 2D/2D Heterojunction of Ultrathin MXene/$Bi_2WO_6$ Nanosheets for Improved Photocatalytic $CO_2$ Reduction, *Adv. Funct. Mater.*, 2018, **28**, 1800136.
13 S. Xie, Y. Wang, Q. Zhang, W. Deng and Y. Wang, $SrNb_2O_6$ nanoplates as efficient photocatalysts for the preferential reduction of $CO_2$ in the presence of $H_2O$, *Chem. Commun.*, 2015, **51**, 3430–3433.
14 S. R. Lingampalli, M. M. Ayyub, G. Magesh and C. N. R. Rao, Photocatalytic reduction of $CO_2$ by employing ZnO/$Ag_{1-x}Cu_x$/CdS and related heterostructures, *Chem. Phys. Lett.*, 2018, **691**, 28–32.

 

15 K. Li, B. Peng and T. Peng, Recent Advances in Heterogeneous Photocatalytic $CO_2$ Conversion to Solar Fuels, *ACS Catal.*, 2016, **6**, 7485–7527.
16 H. Yang, B. Yang, W. Chen and J. Yang, Preparation and Photocatalytic Activities of $TiO_2$-Based Composite Catalysts, *Catalysts*, 2022, **12**, 1263.
17 M. Ge, C. Cao, J. Huang, S. Li, Z. Chen, K. Zhang, S. S. AlDeyabd and Y. Lai, A review of one-dimensional $TiO_2$ nanostructured materials for environmental and energy applications, *J. Mater. Chem. A*, 2016, **4**, 6772–6801.
18 R. Asahi, T. Morikawa, T. Ohwaki, K. Aoki and Y. Taga, Visible-Light Photocatalysis in Nitrogen-Doped Titanium Oxides, *Science*, 2001, **293**, 269.
19 V. Subramanian, E. E. Wolf and P. V. Kamat, Catalysis with $TiO_2$/Gold Nanocomposites. Effect of Metal Particle Size on the Fermi Level Equilibration, *J. Am. Chem. Soc.*, 2004, **126**, 4943.
20 X. Zhang, H. Cui, M. Humayun, Y. Qu, N. Fan, X. Sun and L. Jing, Exceptional performance of photoelectrochemical water oxidation of single-crystal rutile $TiO_2$ nanorods dependent on the hole trapping of modified chloride, *Sci. Rep.*, 2016, **6**, 21430.
21 L. Wei, C. Yu, Q. Zhang, H. Liud and Y. Wang, $TiO_2$-based heterojunction photocatalysts for photocatalytic reduction of $CO_2$ into solar fuels, *J. Mater. Chem. A*, 2018, **6**, 22411–22436.
22 R. Marschall, Semiconductor Composites: Strategies for Enhancing Charge Carrier Separation to Improve Photocatalytic Activity, *Adv. Funct. Mater.*, 2014, **24**, 2421–2440.
23 T. Kawahara, Y. Konishi, H. Tada, N. Tohge, J. Nishii and S. Ito, A Patterned $TiO_2$(Anatase)/$TiO_2$(Rutile) Bilayer-Type Photocatalyst: Effect of the Anatase/Rutile Junction on the Photocatalytic Activity, *Angew. Chem.*, 2002, **114**, 2935.
24 M.-G. Ju, G. Sun, J. Wang, Q. Meng and W. Liang, Origin of High Photocatalytic Properties in the Mixed-Phase $TiO_2$: A First-Principles Theoretical Study, *ACS Appl. Mater. Interfaces*, 2014, **6**, 12885–12892.
25 X. Wang, Q. Xu, M. Li, S. Shen, X. Wang, Y. Wang, Z. Feng, J. Shi, H. Han and C. Li, Photocatalytic overall water splitting promoted by an α-β phase junction on $Ga_2O_3$, *Angew. Chem., Int. Ed.*, 2012, **51**, 13089.
26 K. Afroz, M. Moniruddin, N. Bakranov, S. Kudaibergenov and N. Nuraje, A heterojunction strategy to improve the visible light-sensitive water-splitting performance of photocatalytic materials, *J. Mater. Chem. A*, 2018, **6**, 21696–21718.
27 J. Low, J. Yu, M. Jaroniec, S. Wageh and A. A. Al-Ghamdi, Heterojunction Photocatalysts, *Adv. Mater.*, 2017, 1601694.
28 R. T. Ross and T.-L. Hsiao, Limits on the yield of photochemical solar energy conversion, *J. Appl. Phys.*, 1977, **48**, 4783–4785.
29 M. C. Hanna and A. J. Nozik, Solar conversion efficiency of photovoltaic and photoelectrolysis cells with carrier multiplication absorbers, *J. Appl. Phys.*, 2006, **100**, 074510.
30 M. R. Singh, E. L. Clark and A. T. Bell, Thermodynamic and achievable efficiencies for solar-driven electrochemical reduction of carbon dioxide to transportation fuels, *Proc. Natl. Acad. Sci. U. S. A.*, 2015, **112**, E6111–E6118.
31 A. Paracchino, V. Laporte, K. Sivula, M. Gratzel and E. Thimsen, Highly active oxide photocathode for hotoelectrochemical water reduction, *Nat. Mater.*, 2011, **10**, 456–461.
32 C. Sotelo-Vazquez, R. Quesada-Cabrera, M. Ling, D. O. Scanlon, A. Kafizas, P. K. Thakur, T.-L. Lee, A. Taylor, G. W. Watson, R. G. Palgrave, J. R. Durrant, C. S. Blackman and I. P. Parkin, Evidence and Effect of Photogenerated Charge Transfer for Enhanced Photocatalysis in $WO_3$/$TiO_2$ Heterojunction Films: A Computational and Experimental Study, *Adv. Funct. Mater.*, 2017, **27**, 1605413.
33 S. Higashimoto, M. Sakiyama and M. Azuma, Photoelectrochemical properties of hybrid $WO_3$/$TiO_2$ electrode. Effect of structures of $WO_3$ on charge separation behavior, *Thin Solid Films*, 2006, **503**, 201–206.
34 W. Smith, A. Wolcott, R. C. Fitzmorris, J. Z. Zhang and Y. Zhao, Quasi-core-shell $TiO_2$/$WO_3$ and $WO_3$/$TiO_2$ nanorod arrays fabricated by glancing angle deposition for solar water splitting, *J. Mater. Chem.*, 2011, **21**, 10792–10800.
35 Z. Chen and Y.-J. Xu, Ultrathin $TiO_2$ Layer Coated-CdS Spheres Core-Shell Nanocomposite with Enhanced Visible-Light Photoactivity, *ACS Appl. Mater. Interfaces*, 2013, **5**, 13353–13363.
36 H. Ge, F. Xu, B. Cheng, J. Yu and W. Ho, S-Scheme Heterojunction $TiO_2$/CdS Nanocomposite Nanofiber as H2- Production Photocatalyst, *ChemCatChem*, 2019, **11**, 6301–6309.
37 F. Xu, K. Meng, B. Cheng, S. Wang, J. Xu and J. Yu, Unique Sscheme heterojunctions in self-assembled $TiO_2$/$CsPbBr_3$ hybrids for $CO_2$ photoreduction, *Nat. Commun.*, 2020, **11**, 4613.
38 A. Ennaoui, S. Fiechter, C. Pettenkofer, N. Alonso-Vante, K. Büker, M. Bronold, C. Höpfner and H. Tributsch, Iron Disulfide for Solar Energy Conversion, *Sol. Energy Mater. Sol. Cells*, 1993, **29**, 289–370.
39 D.-Y. Wang, C.-H. Li, S.-S. Li, T.-R. Kuo, C.-M. Tsai, T. R. Chen, Y.-C. Wang, C.-W. Chen and C.-C. Chen, Iron Pyrite/Titanium Dioxide Photoanode for Extended Near Infrared Light Harvesting in a Photoelectrochemical Cell, *Sci. Rep.*, 2016, **6**, 20397.
40 L. Wu, N. Y. Dzade, L. Gao, D. O. Scanlon, Z. Öztürk, N. Hollingsworth, B. M. Weckhuysen, E. J. M. Hensen, N. H. de Leeuw and J. P. Hofmann, Enhanced Photoresponse of $FeS_2$ Films: The Role of Marcasite–Pyrite Phase Junctions, *Adv. Mater.*, 2016, **28**, 9602–9607.
41 E. Han, F. Hu, S. Zhang, B. Luan and P. Li, Hongqi Sun, and Shaobin Wang. Worm-like FeS2/TiO2 Nanotubes for Photoelectrocatalytic Reduction of $CO_2$ to Methanol under Visible Light, *Energy Fuels*, 2018, **32**, 4357–4363.
42 T.-R. Kuo, H.-J. Liao, Y.-T. Chen, C.-Y. Wei, C.-C. Chang, Y.-C. Chen, Y.-H. Chang, J.-C. Lin, Y.-C. Lee, C.-Y. Wen, S.-S. Li, K.-H. Lin and D.-Y. Wang, Extended visible to near-infrared harvesting of earth-abundant $FeS_2$–$TiO_2$ heterostructures for highly active photocatalytic hydrogen evolution, *Green Chem.*, 2018, **20**, 1640–1647.
43 Z. Chen, R. Zheng, S. Deng, W. Wei, W. Wei, B.-J. Ni and H. Chen, Modular design of an efficient heterostructured $FeS_2$/$TiO_2$ oxygen evolution electrocatalyst via sulfidation of natural ilmenites, *J. Mater. Chem. A*, 2021, **9**, 25032–25041.

44 J. Rashid, S. Saleem, S. U. Awan, A. Iqbal, R. Kumar, M. A. Barakat, M. Arshad, M. Zaheer, M. Rafique and M. Awad, Stabilized fabrication of anatase-$TiO_2$/$FeS_2$ (pyrite) semiconductor composite nanocrystals for enhanced solar light-mediated photocatalytic degradation of methylene blue, *RSC Adv.*, 2018, **8**, 11935–11945.

45 G. Lee and M. Kang, Physicochemical properties of core/shell structured pyrite $FeS_2$/anatase $TiO_2$ composites and their photocatalytic hydrogen production performances, *Curr. Appl. Phys.*, 2013, **13**, 1482–1489.

46 Y. Xin, L. Li, W. Wu, F. Fu and Z. Zhang, Pyrite $FeS_2$ Sensitized $TiO_2$ Nanotube Photoanode for Boosting Near-Infrared Light Photoelectrochemical Water Splitting, *ACS Sustainable Chem. Eng.*, 2016, **4**(12), 6659–6667.

47 P. E. Blöchl, Projector augmented-wave method, *Phys. Rev. B: Condens. Matter Mater. Phys.*, 1994, **50**, 17953–17979.

48 G. Kresse and D. Joubert, From ultrasoft pseudopotentials to the projector augmented-wave method, *Phys. Rev. B: Condens. Matter Mater. Phys.*, 1999, **59**, 1758–1775.

49 G. Kresse and J. Furthmüller, Efficiency of ab-initio total energy calculations for metals and semiconductors using a plane-wave basis set, *Comput. Mater. Sci.*, 1996, **6**, 15–50.

50 J. P. Perdew, K. Burke and M. Ernzerhof, Generalized Gradient Approximation Made Simple, *Phys. Rev. Lett.*, 1996, **77**, 3865–3868.

51 S. Grimme, J. Antony, S. Ehrlich and H. Krieg, A Consistent and Accurate Ab Initio Parametrization of Density Functional Dispersion Correction (DFT-D) for the 94 Elements H–Pu, *J. Chem. Phys.*, 2010, **132**, 154104.

52 H. J. Monkhorst and J. D. Pack, Special points for Brillouin-zone integrations, *Phys. Rev. B: Condens. Matter Mater. Phys.*, 1976, **13**, 5188–5192.

53 S. L. Dudarev, G. A. Botton, S. Y. Savrasov, C. J. Humphreys and A. P. Sutton, Electron-energy-loss spectra and the structural stability of nickel oxide: An LSDA + U study, *Phys. Rev. B: Condens. Matter Mater. Phys.*, 1998, **57**, 1505–1509.

54 D. R. Alfonso, Computational investigation of $FeS_2$ surfaces and prediction of effects of sulfur environment on stabilities, *J. Phys. Chem. C*, 2010, **114**, 8971–8980.

55 L. Chu, Z. Qin, J. Yang and X. Li, Anatase $TiO_2$ Nanoparticles with Exposed {001} Facets for Efficient Dye-Sensitized Solar Cells, *Sci. Rep.*, 2015, **5**, 12143.

56 G. Makov and M. C. Payne, Periodic boundary conditions in ab initio calculations, *Phys. Rev. B: Condens. Matter Mater. Phys.*, 1995, **51**, 4014.

57 W. Tang, E. Sanville and G. Henkelman, A grid-based Bader analysis algorithm without lattice bias, *Phys. Condens. Matter*, 2009, **21**, 084204.

58 M. S. Schmøkel, L. Bjerg, S. Cenedese, M. R. V. Jørgensen, Y.-S. Chen, J. Overgaarda and B. B. Iversen, Atomic properties and chemical bonding in the pyrite and marcasite polymorphs of $FeS_2$: a combined experimental and theoretical electron density study, *Chem. Sci.*, 2014, **5**, 1408–1421.

59 F. Hulliger and E. Mooser, Semiconductivity in pyrite, marcasite and arsenopyrite phases, *J. Phys. Chem. Solids*, 1965, **26**, 429–433.

60 G. Brostigen and A. Kjekshus, On the relationships between the structure types pyrite, marcasite, and arsenopyrite, *Acta Chem. Scand.*, 1970, **24**, 2983–2992.

61 M. L. Huggins, The crystal structures of marcasite ($FeS_2$), arsenopyrite (FeAsS) and loellingite ($FeAs_2$), *Phys. Rev.*, 1922, **19**, 369–373.

62 G. Brostigen and A. Kjekshus, Redetermined crystal structure of $FeS_2$ (Pyrite), *Acta Chem. Scand.*, 1969, **23**, 2186–2188.

63 R. Murphy and D. R. Strongin, Surface reactivity of pyrite and related sulfides, *Surf. Sci. Rep.*, 2009, **64**, 1–45.

64 R. Sun, M. K. Y. Chan and G. Ceder, First-principles electronic structure and relative stability of pyrite and marcasite: Implications for photovoltaic performance, *Phys. Rev. B: Condens. Matter Mater. Phys.*, 2011, **83**, 235311.

65 P. Xiao, X.-L. Fan, L.-M. Liu and W.-M. Lau, Band gap engineering of $FeS_2$ under biaxial strain: a first principles study, *Phys. Chem. Chem. Phys.*, 2014, **16**, 24466–24472.

66 J. Hu, Y. Zhang, M. Law and R. Wu, First-principles studies of the electronic properties of native and substitutional anionic defects in bulk iron pyrite, *Phys. Rev. B: Condens. Matter Mater. Phys.*, 2012, **85**, 085203.

67 T. Rozgonyi and A. Stirling, DFT Study of Oxidation States on Pyrite Surface Sites, *J. Phys. Chem. C*, 2015, **119**, 7704–7710.

68 P. H. L. Sit, M. H. Cohen and A. Selloni, Interaction of Oxygen and Water with the (100) Surface of Pyrite: Mechanism of Sulfur Oxidation, *J. Phys. Chem. Lett.*, 2012, **3**, 2409–2414.

69 D. T. Cromer and K. Herrington, The Structures of Anatase and Rutile, *J. Am. Chem. Soc.*, 1955, **77**(18), 4708–4709.

70 C. J. Howard, T. M. Sabine and F. Dickson, Structural and thermal parameters for rutile and anatase, *Acta Crystallogr., Sect. B: Struct. Sci.*, 1991, **47**, 462–468.

71 T. Schena, G. Bihlmayer and S. Blügel, First-principles studies of $FeS_2$ using many-body perturbation theory in the $G_0W_0$ approximation, *Phys. Rev. B: Condens. Matter Mater. Phys.*, 2013, **88**, 235203.

72 A. Schlegel and P. Wachter, Optical Properties, Phonons and Electronic Structure of Iron Pyrite (FeS2), *J. Phys. C: Solid State Phys.*, 1976, **9**, 3363–3369.

73 A. Zaka, S. M. Alhassan and A. Nayfeh, Iron pyrite in photovoltaics: a review on recent trends and challenges, *ACS Appl. Electron. Mater.*, 2022, **4**, 4173–4211.

74 L. Kavan, M. Grätzel, S. E. Gilbert, C. Klemenz and H. J. Scheel, Electrochemical and photoelectrochemical investigation of single-crystal anatase, *J. Am. Chem. Soc.*, 1996, **118**, 6716–6723.

75 T. Liu, I. Temprano, S. J. Jenkins, D. A. King and S. M. Driver, Nitrogen adsorption and desorption at iron pyrite $FeS_2$(100) surfaces, *Phys. Chem. Chem. Phys.*, 2012, **14**, 11491–11499.

76 M. Sacchi, M. C. E. Galbraith and S. J. Jenkins, The interaction of iron pyrite with oxygen, nitrogen and nitrogen oxides: a first-principles study, *Phys. Chem. Chem. Phys.*, 2012, **14**, 3627–3633.

77 F. Xiong, L.-L. Yin, F. Li, Z. Wu, Z. Wang, G. Sun, H. Xu, P. Chai, X.-Q. Gong and W. Huang, Anatase TiO2(001)-(1 × 4)

 

Surface Is Intrinsically More Photocatalytically Active than the Rutile TiO2(110)-(1 × 1) Surface, *J. Phys. Chem. C*, 2019, **123**(40), 24558–24565.

78 H. Sun, W. Lu and J. Zhao, Structure and Reactivity of Anatase $TiO_2$(001)-(1 × 4) Surface, *J. Phys. Chem. C*, 2018, **122**, 14528–14536.

79 H. Xian, J. Zhu, X. Liang and H. He, Morphology controllable syntheses of micro- and nano-iron pyrite mono- and poly-crystals: a review, *RSC Adv.*, 2016, **6**, 31988–31999.

80 S. Yang, N. Huang, Y. M. Jin, H. Q. Zhang, Y. H. Su and H. G. Yang, Crystal shape engineering of anatase $TiO_2$ and its biomedical applications, *CrystEngComm*, 2015, **17**, 6617–6631.

81 L. Samad, M. Cabán-Acevedo, M. J. Shearer, K. Park, R. J. Hamers and S. Jin, Direct Chemical Vapor Deposition Synthesis of Phase-Pure Iron Pyrite ($FeS_2$) Thin Films, *Chem. Mater.*, 2015, **27**, 3108–3114.

82 G. Xiong, R. Shao, T. C. Droubay, A. G. Joly, K. M. Beck, S. A. Chambers and W. P. Hess, Photoemission electron microscopy of $TiO_2$ anatase films embedded with rutile nanocrystals, *Adv. Funct. Mater.*, 2007, **17**, 2133–2138.

83 E. Cerrato, C. Gionco, M. C. Paganini, E. Giamello, E. Albanese and G. Pacchioni, Origin of Visible Light Photoactivity of the $CeO_2$/ZnO Heterojunction, *ACS Appl. Energy Mater.*, 2018, **1**, 4247–4260.

84 C. G. Van de Walle and R. M. Martin, Theoretical study of band offsets at semiconductor interfaces, *Phys. Rev. B: Condens. Matter Mater. Phys.*, 1987, **35**, 8154–8165.

85 L. Weston, H. Tailor, K. Krishnaswamy, L. Bjaalie and C. G. Van de Walle, Accurate and efficient band-offset calculations from density functional theory, *Comput. Mater. Sci.*, 2018, **151**, 174–180.

86 L. Kleinman, Comment on the average potential of a Wigner solid, *Phys. Rev. B: Condens. Matter Mater. Phys.*, 1981, **24**, 7412.

87 J. Jia, Y. Li, B. Yao, Z. Ding, R. Deng, Y. Jiang and Y. Sui, Band offsets of $Ag_2ZnSnSe_4$/CdS heterojunction: An experimental and first-principles study, *J. Appl. Phys.*, 2017, **121**, 215305.

88 G. Di Liberto, S. Tosoni, F. Illas and G. Pacchioni, Nature of $SrTiO_3/TiO_2$ (anatase) heterostructure from hybrid density functional theory calculations, *J. Chem. Phys.*, 2020, **152**, 184704.

89 M. A. Sha, P. C. Meenu, V. S. Sumi, T. C. Bhagya, B. R. Sreelekshmy and S. M. A. Shibli, Tuning of electron transfer by Ni–P decoration on $CeO_2$–$TiO_2$ heterojunction for enhancement in photocatalytic hydrogen generation, *Mater. Sci. Semicond. Process.*, 2020, **105**, 104742.

90 Y. Liao, P. Deng, X. Wang, D. Zhang, F. Li, Q. Yang, H. Zhang and Z. Zhong, A facile method for preparation of $Cu_2O$–$TiO_2$ NTA heterojunction with visible-photocatalytic activity, *Nanoscale Res. Lett.*, 2018, **13**, 221.